A robust model of smoldering-driven pyrolysis reactor – Part 1: Thermal performance evaluation

Ruming Pan, Gerald Debenest

A robust model of smoldering-driven pyrolysis reactor – Part 1: Thermal performance evaluation

Ruming Pan [a,*], Gérald Debenest [a]

[a] Institut de Mécanique des Fluides de Toulouse (IMFT) - Université de Toulouse, CNRS-INPT-UPS, Toulouse 31400, France

Corresponding Author *E-mails: ruming.pan@toulouse-inp.fr

Abstract

This study numerically investigates a smoldering-driven pyrolysis reactor. The reactor consists of two chambers: the smoldering chamber for the contaminated sand remediation and the pyrolysis chamber for the waste valorization. This study aims to develop a numerical model to verify the feasibility of the reactor and evaluate its thermal performance. The findings reveal that the contaminant (char) in the sand can be destroyed via smoldering and that the process can be self-sustaining after ignition. It is noteworthy that the ignition requires external energy input. Smoldering can produce a heatwave with a stable peak temperature and propagation velocity. The heatwave generated in the smoldering chamber can heat the pyrolysis chamber through the boundary. The results highlight that the reactor's pivotal operating characteristics (peak temperature, ignition time, and reaction duration) can be regulated by the critical parameters (char concentration, air inlet velocity, and oxygen concentration).

Keywords

22 Smoldering; Remediation; Numerical model; Ignition; Thermal performance.

23

24 **Nomenclature**

Latin letters	
A	Pre-exponential factor, s^{-1}
A_s	Surface area, m^2
C	Concentration, %
C_p	Specific heat capacity, $J\cdot(kg\cdot K)^{-1}$
d	Thickness, m
D	Diffusion coefficient, $m^2\cdot s^{-1}$
d_p	Particle diameter, m
E	Activation energy, $kJ\cdot mol^{-1}$
h_{sg}	Interfacial heat transfer coefficient, $W\cdot m^{-2}\cdot K^{-1}$
k	Thermal conductivity, $W\cdot m^{-1}\cdot K^{-1}$
k_p	Permeability, m^2
m	Mass, kg
M	Molecular weight, $g\cdot mol^{-1}$
n	Axial vector
Nu	Nusselt number
p	Pressure, Pa
Pr	Prandtl number
q	Heat flux, $W\cdot m^{-2}$
R	Reaction rate, s^{-1}
Re	Reynolds number
R_g	Ideal gas constant, $J\cdot mol^{-1}\cdot K^{-1}$
t	Time (duration), s
t_g	Time to start air supply, s
t_h	Time to turn off the heater, s
T	Temperature, °C
u	Velocity, $m\cdot s^{-1}$
v	Stoichiometric coefficient
Y	Mass fraction
Greek symbols	
ΔH	Enthalpy of reaction, $MJ\cdot kg^{-1}$
ρ	Density, $kg\cdot m^{-3}$
ε_p	Porosity
σ	Stefan–Boltzmann constant, $W\cdot m^{-2}\cdot K^{-4}$
μ	Dynamic viscosity, Pa·s
Subscripts/superscript	

bed	Bed material in pyrolysis chamber
eff	Effective
f	Fluid in pyrolysis chamber
g	Gases in smoldering chamber
in	Inlet
ins	Insulation
0	Initial
O_2	Oxygen
p	Peak value
py	Pyrolysis
rad	Radiation
s	Solid in smoldering chamber
smo	Smoldering
sp	Sphere
ss	Stainless steel
∞	Ambient

1. Introduction

Smoldering is flameless combustion that occurs in a porous medium, allowing sufficient oxygen diffusion [1-2]. Smoldering can self-sustain when the heat production rate exceeds the heat loss rate [3]. Self-sustaining smoldering is increasingly popular for treating contaminated soils/sands [4], disposing of wastes [5-6], and realizing waste valorization [7-10]. The contaminants (fuels) (e.g., char [11], bitumen [12], peat moss [13], oil [14]) in the soils/sands can be destroyed by reacting with oxygen, which is a process that releases intensive heat. The smoldering heat can be used for waste disposal and valorization [15].

The smoldering reactor for waste treatment can be classified as in-situ and ex-situ types. The in-situ reactor refers to the smoldering and waste treatment occurring in the same chamber. In many cases, the waste can be combusted with oxygen to provide sufficient heat for self-sustaining smoldering [16-19]. However, it is necessary to add fuel to the reactor to increase

38 the heat generated by smoldering to avoid quenching if the waste solely combustion does not
39 generate enough heat [20-21]. On the other hand, the ex-situ reactor refers to the smoldering
40 and waste treatment occurring in two chambers [5,15]. The smoldering heat is transferred to the
41 waste treatment chamber through the boundary between the two chambers.

42 The fuel concentration or contaminant saturation is regarded as one of the most critical
43 parameters in the self-sustaining smoldering process [12]. Higher fuel concentrations in the
44 presence of sufficient oxygen supply increase the oxidation rate, thereby releasing more
45 intensive heat and enhancing the local (smoldering front) energy out rate, leading to an increase
46 in the peak temperature and propagation velocity [12]. The air flow is another critical parameter
47 regulating the smoldering characteristics. Generally, increasing the air flow rate can make it
48 more facilitative for smoldering to propagate [20]. Moreover, the oxygen concentration can also
49 regulate the smoldering combustion by controlling the local reaction rate [22].

50 On the other hand, pyrolysis or thermal decomposition in an inert atmosphere is a promising
51 technology for waste treatment since it can convert waste into value-added fuels [23-26]. Since
52 smoldering needs oxygen consumption whereas pyrolysis demands oxygen-free, the
53 smoldering-driven pyrolysis reactor should be of the ex-situ type [15]. However, most
54 smoldering studies are performed in-situ, and only a few focus on the ex-situ applications
55 [5,15,27]. Moreover, the numerical study for the smoldering-driven pyrolysis reactor remains
56 vacant to the best of our knowledge.

57 Due to the lack of applications of ex-situ smoldering for waste pyrolysis, this study develops
58 a robust numerical model for the smoldering-driven pyrolysis reactor. The reactor consists of a

smoldering chamber for contaminated sand remediation and a pyrolysis chamber for waste valorization. This study highlights the feasibility and thermal performance of the smoldering-driven pyrolysis reactor. Firstly, the two-dimensional smoldering model is verified according to the experimental results. Then, the reactor's crucial thermal characteristics (e.g., ignition time, smoldering duration, and peak temperature) are evaluated under the critical operating parameters (e.g., fuel concentration, air inlet velocity, and oxygen concentration). The model presented in this study aims to provide a general tool to evaluate the thermal performance of the smoldering-driven pyrolysis reactor, which is used for contaminated sand/soil remediation and waste pyrolysis.

2. Methodology

2.1.Reactor description

Fig. 1 demonstrates the schematic of the smoldering-driven pyrolysis reactor. The reactor consists of a smoldering chamber and a pyrolysis chamber. The smoldering chamber is filled with a mixture of sand and char, with a 2.0–2.8% char concentration. The mixture in the smoldering chamber can be regarded as contaminated sand. The bottom of the reaction chamber is equipped with quartz glass, which enables the cone heater to heat the mixture and ignite the char. The cone heater is turned off when the char is ignited. The char ignition indicates that the smoldering can self-sustainingly propagate without the external energy input. The ignition is manifested in the appearance of solid temperature hot spots. Therefore, the ignition temperature is defined as the temperature of hot spots in this study. Air is introduced into the smoldering

chamber by the air pump after heating for 1020s. Heat loss is reduced by an insulation layer (ceramic fiber [28]) with a thickness of 0.01m on the outside of the smoldering chamber.

The smoldering chamber is made of stainless steel with a thickness of 2mm. Its interior is a porous medium with high thermal conductivity, enabling a uniform radial temperature distribution. The pyrolysis chamber is heated by the internal boundary heat flux of the smoldering chamber.

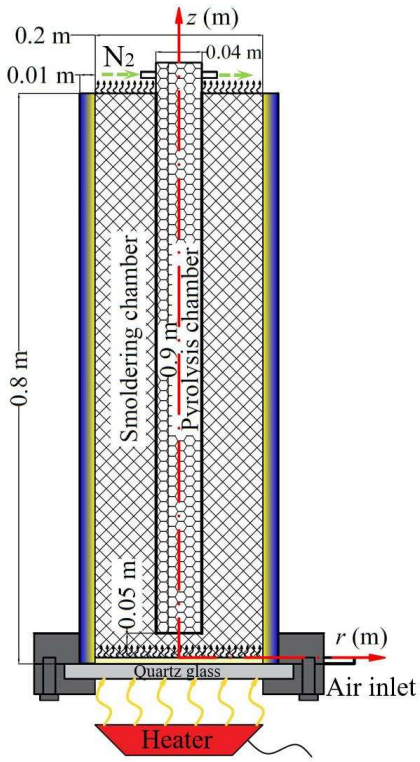

Fig. 1. Illustration of smoldering-driven pyrolysis reactor.

Table 1 shows the designed scenarios for the thermal performance evaluation of the smoldering-driven pyrolysis reactor in this study.

Table 1. Designed scenarios for thermal performance evaluation of smoldering-driven pyrolysis reactor.

Case	Char concentration (%)	Air inlet velocity (m/s)	Oxygen concentration (%)
1 [a]	2.0	0.03	20.4
2 [b]	2.2	0.03	20.4
3 [b]	2.4	0.03	20.4

4 [b]	2.6	0.03	20.4
5 [b]	2.8	0.03	20.4
6 [c]	2.0	0.04	20.4
7 [c]	2.0	0.05	20.4
8 [c]	2.0	0.06	20.4
9 [c]	2.0	0.07	20.4
10 [d]	2.0	0.03	10
11 [d]	2.0	0.03	15
12 [d]	2.0	0.03	25
13 [d]	2.0	0.03	30

[a] Base case.

[b] Study on the effect of char concentration.

[c] Study on the effect of air inlet velocity.

[d] Study on the effect of oxygen concentration.

2.2.Governing equations

The governing equations for the mass conservations of char and air in the smoldering chamber are given by:

$$\frac{\partial}{\partial t}(Y_{Char}) = -R_{Char} \tag{1}$$

$$\frac{\partial}{\partial t}(\varepsilon_{p,smo}\rho_g) + \nabla \cdot (\rho_g \mathbf{u_g}) = \rho_{Char} R_{Char} \tag{2}$$

where the char oxidation rate is determined by the Arrhenius expression $R_{Char} = A_{Char}\exp(-E_{Char}/(R_g T_s))Y_{Char}Y_{O_2}$, the porosity of smoldering chamber is $\varepsilon_{p,smo} = \varepsilon_{p,smo,0}(1 - Y_{Char}C_{Char})$, and the air velocity follows the Darcy's Law $\mathbf{u_g} = -(\kappa_{p,smo}/\mu_g)\nabla p_g$.

The oxygen transport equation in the smoldering chamber can be expressed as follows.

$$\frac{\partial}{\partial t}(\varepsilon_{p,smo}\rho_g Y_{O_2}) + \nabla \cdot (\rho_g \mathbf{u_g} Y_{O_2}) = \nabla \cdot (\varepsilon_{p,smo}\rho_g D_g \nabla Y_{O_2}) - \rho_{Char} v_{O_2} R_{Char} \tag{3}$$

The governing equations for the energy conservations of char and air in the smoldering chamber are given by the following equations.

$$\frac{\partial(\rho C_p)_{eff,smo}T_s}{\partial t} = \nabla \cdot \left(k_{eff,smo}\nabla T_s\right) + h_{sg}(A_{s,sp}/V_{sp})(T_g - T_s) - \rho_{Char}\Delta H_{Char}R_{Char} \quad (4)$$

$$\frac{\partial \varepsilon_{p,smo}(\rho_g C_{p,g})T_g}{\partial t} + \nabla \rho_g C_{p,g}\mathbf{u_g}T_g = \nabla \cdot \left(\varepsilon_{p,smo}k_g \nabla T_g\right) + h_{sg}(A_{s,sp}/V_{sp})(T_s - T_g) \quad (5)$$

where the interfacial heat transfer coefficient h_{sg} is determined by $Nu = h_{sg}d_{p,Sand}/k_g = 0.001(Re^{1.97}Pr^{1/3})$ [11], the surficial area per unit volume $A_{s,sp}/V_{sp} = 6(1-\varepsilon_{p,smo})/d_{p,Sand}$ [12], and the solid (sand and char) effective volumetric heat capacity $(\rho C_p)_{eff,smo}$ and effective thermal conductivity $k_{eff,smo}$ are defined as:

$$(\rho C_p)_{eff,smo} = \left(1-\varepsilon_{p,smo,0}\right)\rho_{Sand}C_{p,Sand} + Y_{Char}\rho_{Char}C_{p,Char} \quad (6)$$

$$k_{eff,smo} = \left(1-\varepsilon_{p,smo,0}\right)(k_{Sand} + k_{rad,smo}) + Y_{Char}C_{Char}\varepsilon_{p,smo,0}k_{Char} \quad (7)$$

where the radiation heat transfer is expressed as a radiative conductivity and follows the Rosseland approximation ($k_{rad,smo} = 16\sigma d_{p,Sand}{T_s}^3/3$) [29-30].

The mass, momentum and energy conservations in the pyrolysis chamber are given by the following equations.

$$\frac{\partial}{\partial t}\left(\varepsilon_{p,py}\rho_f\right) + \nabla \cdot (\rho_f \mathbf{u_f}) = 0 \quad (8)$$

$$\mathbf{u_f} = -\frac{\kappa_{p,py}}{\mu_f}\nabla p_f \quad (9)$$

$$\frac{\partial(\rho C_p)_{eff,py}T_{py}}{\partial t} + \nabla \cdot ((\rho C_p)_{eff,py}\mathbf{u_f}T_{py}) = \nabla \cdot \left(k_{eff,py}\nabla T_{py}\right) \quad (10)$$

where the effective $(\rho C_p)_{eff,py}$ and $k_{eff,py}$ in the pyrolysis chamber are given by:

$$(\rho C_p)_{eff,py} = \left(1-\varepsilon_{p,py}\right)\rho_{bed}C_{p,bed} + \varepsilon_{p,py}\rho_f C_{p,f} \quad (11)$$

$$k_{eff,py} = \left(1-\varepsilon_{p,py}\right)(k_{bed} + k_{rad,py}) + \varepsilon_{p,py}k_f \quad (12)$$

where the radiation heat transfer coefficient $k_{rad,py} = 16\sigma d_{p,bed}{T_{py}}^3/3$.

2.3.Boundary and initial conditions

Fig. 2 shows the boundary conditions of the numerical model. It is noteworthy that there is only heat transfer between the smoldering and pyrolysis chambers, which exchanges through the boundary. The two chambers are separated by stainless steel with a thickness of 2mm. The heat transfer between the two chambers follows the thermally thick approximation [31]:

$$-\mathbf{n}_{smo}\cdot\mathbf{q}_{smo}=-\frac{1}{2}d_{ss}\rho_{ss}C_{p,ss}\frac{\partial T_s}{\partial t}-\frac{T_{py}-T_s}{d_{ss}/k_{ss}} \tag{13}$$

$$-\mathbf{n}_{py}\cdot\mathbf{q}_{py}=-\frac{1}{2}d_{ss}\rho_{ss}C_{p,ss}\frac{\partial T_{py}}{\partial t}-\frac{T_s-T_{py}}{d_{ss}/k_{ss}} \tag{14}$$

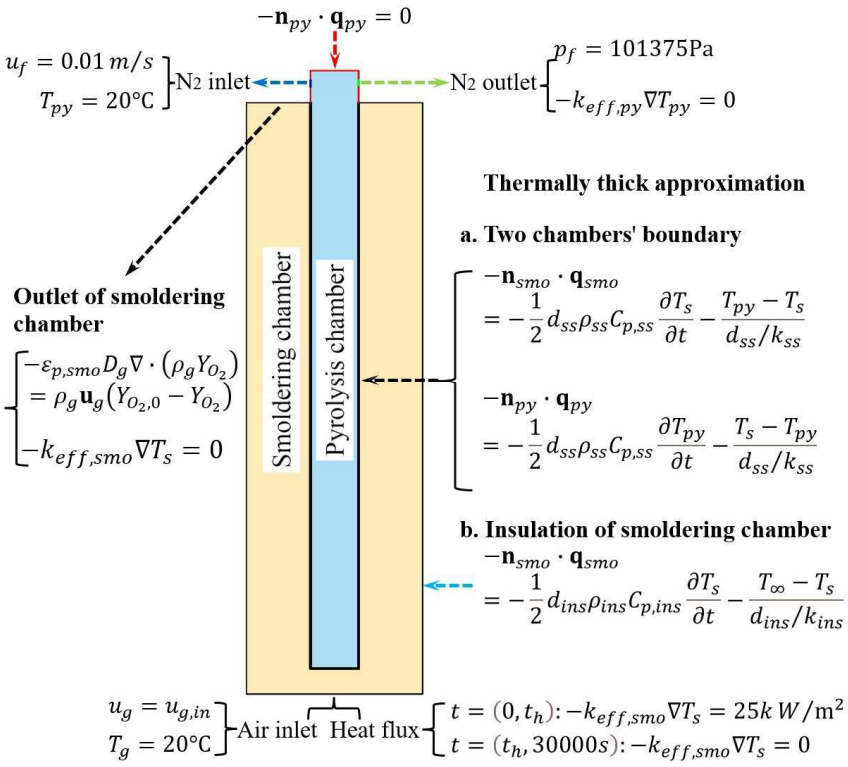

Fig. 2. Boundary conditions of the numerical model.

The thermally thick approximation can address the role of insulation thickness in the boundary heat loss assessment [32]. Additional initial and boundary conditions are tabulated in Table 2. The model inputs and materials' physical parameters are listed in Table 3.

Table 2. Initial and boundary conditions.

Initial Condition	Boundary Condition
Smoldering chamber	
t=0s: $Y_{Char}=1$	-

t=0s: $p_g = 101375\text{Pa}$	z=0.00m:	$\begin{cases} t = (0, t_g): u_g = 0 \\ t = (t_g, 30000s): u_g = u_{g,in} \end{cases}$
	z=0.80m:	$p_g = 101375\text{Pa}$
t=0s: $Y_{O_2} = 0.204$	z=0.00m:	$Y_{O_2} = 0.204$
	z=0.80m:	$-\varepsilon_{p,smo} D_g \nabla \cdot (\rho_g Y_{O_2}) = \rho_g \mathbf{u}_g (Y_{O_2,0} - Y_{O_2})$
t=0s: $T_s = 20°\text{C}$	z=0.00m:	$\begin{cases} t = (0, t_h): -k_{eff,smo} \nabla T_s = 25\text{kW/m}^2 \\ t = (t_h, 30000s): -k_{eff,smo} \nabla T_s = 0 \end{cases}$
	z=0.80m:	$-k_{eff,smo} \nabla T_s = 0$
t=0s: $T_g = 20°\text{C}$	z=0.00m:	$T_g = 20°\text{C}$
	z=0.80m:	$-k_g \nabla T_g = 0$
-	r=0.10m:	$-\mathbf{n}_{smo} \cdot \mathbf{q}_{smo} = -\frac{1}{2} d_{ins} \rho_{ins} C_{p,ins} \frac{\partial T_s}{\partial t} - \frac{T_\infty - T_s}{d_{ins}/k_{ins}}$
Pyrolysis chamber		
t=0s: $p_f = 101375\text{Pa}$	Inlet:	$u_f = 0.01 m/s$
	Outlet:	$p_f = 101375\text{Pa}$
t=0s: $T_{py} = 20°\text{C}$	Inlet:	$T_{py} = 20°\text{C}$
	Outlet:	$-k_{eff,py} \nabla T_{py} = 0$
-	Remaining boundaries:	$-\mathbf{n}_{py} \cdot \mathbf{q}_{py} = 0$

Table 3. Model inputs and materials' physical parameters.

Par.	Value	Unit
Smoldering chamber		
v_{O2}	1.15	-
A_{Char}	707.9	1/s
E_{Char}	68	kJ/mol
ΔH_{Char}	-30.82×10^{3}	kJ/kg
$d_{p,Sand}$	0.88×10^{-3}	m
D_g	4.53×10^{-5}	m^2/s
μ_g	$-9\times10^{-12}(T_g^2)+4\times10^{-8}(T_g)+6\times10^{-6}$	Pa·s
k_{Char}	0.25	W/m/K
k_{Sand}	$0.000541(T_s)+0.1044$	W/m/K
k_g	$-1\times10^{-8}(T_g^2)+8\times10^{-5}(T_g)+4.3\times10^{-3}$	W/m/K
m_{Char}	0.207	kg
m_{Sand}	10.34	kg
C_{Char}	m_{Char}/m_{Sand}=2.0	%
ρ_{Char}	31.80	kg/m^3
ρ_{Sand}	2650	kg/m^3
$C_{p,Char}$	1100	J/kg/K
$C_{p,Sand}$	$2.49(T_s)+39.06$	J/kg/K
$C_{p,g}$	$-3\times10^{-5}(T_g^2)+0.2261\ (T_g)+940.35$	J/kg/K
$\kappa_{p.smo}$	2.54×10^{-10}	m^2

M_g	28.97	g/mol
$\varepsilon_{p,smo,0}$	0.4	-
σ	5.67×10^{-8}	$W/m^2/K^4$
q_{in}	25000	W/m^2
$u_{g,in}$	0.05	m/s
t_g	1020	s
t_h	4320	s
T_∞	293.15	K
Pyrolysis chamber		
$d_{p,bed}$	0.001	m
μ_f	3.0×10^{-5}	Pa·s
k_f	0.02557	W/m/K
k_{bed}	10	W/m/K
$\varepsilon_{p,bed}$	0.4	-
$C_{p,f}$	1100	J/kg/K
$C_{p,bed}$	800	J/kg/K
Boundary		
d_{ins}	0.01	m
d_{ss}	0.002	m
k_{ins}	0.12	W/m/K
k_{ss}	30	W/m/K
ρ_{ins}	150	kg/m^3
ρ_{ss}	7640	kg/m^3
$C_{p,ins}$	1000	J/kg/K
$C_{p,ss}$	530	J/kg/K

3. Results and discussion

3.1.Model verification

Fig. 3 shows the comparison between the experimental [11] and numerical temperature profiles. The experiments were conducted to investigate the smoldering of char and sand mixture. A cone heater heated the reactor for 4320s. The numerical average peak temperature and front velocity were 676°C and 3.00mm/s under C_{Char}=2.0%, and 894°C and 4.79mm/s under C_{Char}=4.0%. Table 4 shows that the numerical results in this study agreed well with the values obtained by Zanoni et al. [11] under C_{Char}=2.0% and C_{Char}=4.0%, with errors equal to

7.74% and 4.14%, respectively. Fig. 3 also demonstrates that the smoldering could self-sustainingly propagate with a stable peak temperature and front velocity. The high temperature generated by smoldering is suitable for the pyrolysis of wastes, e.g., plastics, biomass, and sludge [1].

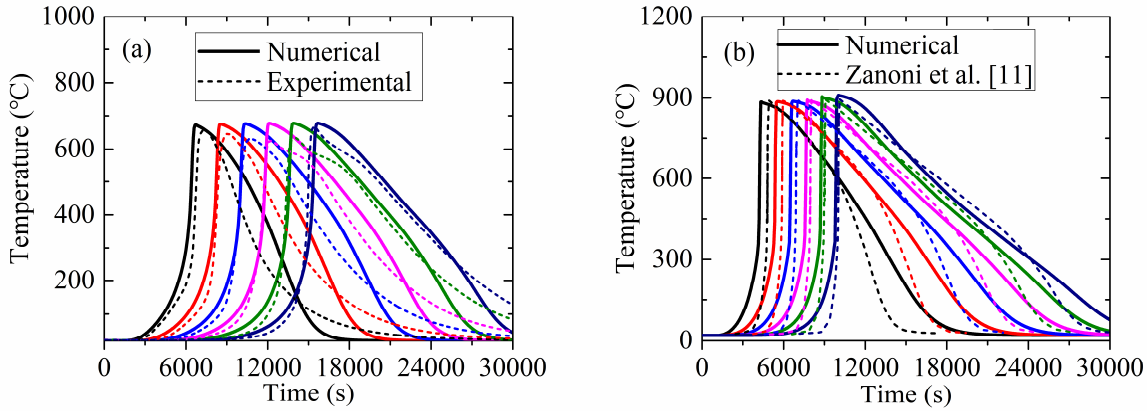

Fig. 3. Experimental and numerical temperature profiles at r=0m and z=0.22–0.67m with 0.09m intervals under $u_{g,in}$=0.05m/s, Y_{O2}=20.4%, (a) C_{Char}=2.0%, and (b) C_{Char}=4.0%.

Table 4. Average peak temperature and front velocity.

C_{Char} \ Comparison	Average peak temperature (°C)			Average front velocity (mm/s)		
	Zanoni et al.	This study	Error	Zanoni et al.	This study	Error
2.0%	643	676	5.08%	3.35	3.00	10.4%
4.0%	893	894	0.20%	5.21	4.79	8.09%

3.2.Reactor thermal assessment

Fig. 4a illustrates that radial temperature distribution in the smoldering chamber is relatively uneven, with a temperature difference (height of light shaded area) of ~274°C. The radial temperature represents the temperature distribution at the same z-axis coordinate. The non-uniform radial temperature distribution is attributed to the low thermal conductivity of sand

(0.26–0.63W/m/K [33]) and the smoldering radial propagation direction (from center to boundary). However, the radial temperature uniformly distributes in the pyrolysis chamber, with a temperature difference (height of dark shaded area) of ~34°C, due to the high conductivity of the porous medium (10W/m/K [34]).

Fig. 4a also shows that the radial-mean peak T_S increases from 612°C to 631°C with time, which can be ascribed to the smoldering heat accumulation in the smoldering chamber [35]. Consequently, the radial-mean peak T_{py} is significantly increased by 98°C (432–530°C) because of the increasing boundary heat flux (Fig. 4b). Fig. 4b indicates that the smoldering occurs in a thin region (~0.05m), resulting in a sharp peak in T_S (Fig. 4a). While the boundary heat flux from the smoldering chamber into the pyrolysis chamber occurs within a wide area (~0.3m), contributing to a flat peak in T_{py}.

As depicted in Fig. 4c, T_S decreases from the smoldering chamber's center to the outer wall ($r: 0 \rightarrow 0.1m$) due to the boundary heat loss [22]. The cone heater heats the sand and char at z=0m, raising the solid temperature T_S. The solid heat propagates forward via conduction, radiation, and convection. The cold air (T_g=20°C) is heated by the solid via convection when introduced into the smoldering chamber. In other words, the solid is cooled by the gas during this stage. The gas will heat the solid by convection when T_g is higher than T_S (preheating zone, Fig. A.1). Fig. 4c indicates that the convective heat transfer plays a critical role in igniting. There are two ignition points at t=2520s due to the change in the velocity field, caused by the structural change of the smoldering chamber (Fig. 1). The heat can self-sustainingly propagate after turning off the cone heater at t=2520s (without the external energy input).

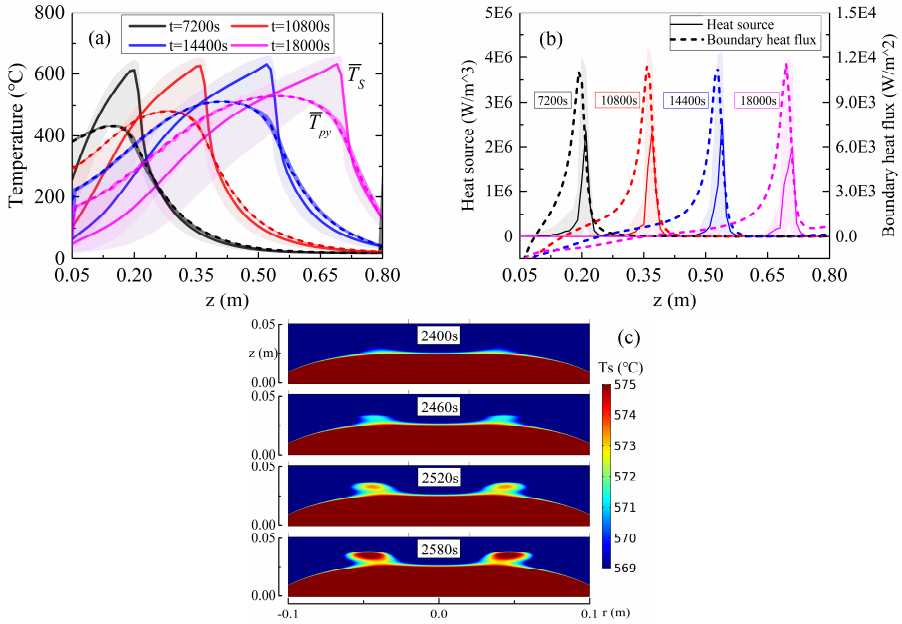

Fig. 4. Smoldering-driven pyrolysis reactor thermal assessment: (a) Longitudinal radial-mean T_s (solid line) and radial-mean T_{py} (dashed line); (b) Longitudinal radial-mean smoldering heat source (solid line) and interface heat flux (dashed line); (c) T_s distributions at t=2400–2580s with 60s intervals.

3.3.Effect of char concentration

Fig. 5a shows that increasing the char concentration shortens the ignition time and increases the ignition temperature. The increment in char concentration leads to an increase in the smoldering heat [36] power density, which reduces the ignition time due to more heat accumulation. Shorter ignition times reveal that higher char concentrations require less external energy input to ignite. It is noteworthy that the ignition indicates that the smoldering can self-sustainingly propagate in the smoldering chamber (Fig. 4c). The higher char concentration raises the temperature during propagation, thus enhancing the ignition temperature. Moreover, there is no significant difference in the ignition locations under different char concentrations, all at z=0.030–0.035m.

Fig. 5b demonstrates that the radial-mean peak T_S significantly increases from 626°C to 712°C when the char concentration increases in the studied range. Accordingly, the radial-mean peak T_{py} is raised by 116°C because of the higher boundary heat flux received by the pyrolysis chamber. It is noteworthy that the heat front is a curved surface (Fig. 4c), and the front temperature is higher than the radial-mean peak T_S. For instance, the radial-mean peak T_S and front temperature at C_{Char}=2.2% are 659°C and 691°C, respectively. The experimental front temperature is 703°C at C_{Char}=2.2% [37], a value very close to the simulated one in this study. Moreover, the heat fronts have been pushed forward by 0.14m (0.36–0.50m) and 0.07m (0.28–0.35m) in the smoldering and pyrolysis chambers when char concentration increases from 2.0% to 2.8% (Fig. 5b), respectively.

As depicted in Fig. 5c, the increment in char concentration increases the peak temperatures (T_S and T_{py}) and propagation velocities ($v_{f,s}$ and $v_{f,py}$). The propagation velocities are determined by tracking the peak temperatures. Increasing the char concentration can enhance the char oxidation rate and provide a more intense heat source. Accordingly, the peak T_S increases at higher char concentrations due to the increased local (smoldering front) net energy rate [12]. Increased local net energy rate results in an increment in the local energy out rate (transferred via convection, conduction, and radiation), leading to a higher propagation velocity. Moreover, the consumed oxygen increases from 4.4% to 7.5% at higher char concentrations (Fig. A.2). The increase in char concentration leads to an increase in the smoldering bed average temperature (Fig. A.3) and an approximately linear increase in the pyrolysis bed average temperature (Fig. 5d), indicating that the pyrolysis bed has received more energy. Moreover,

Fig. 5d reveals that the smoldering duration significantly shortens by 77min at higher char concentrations.

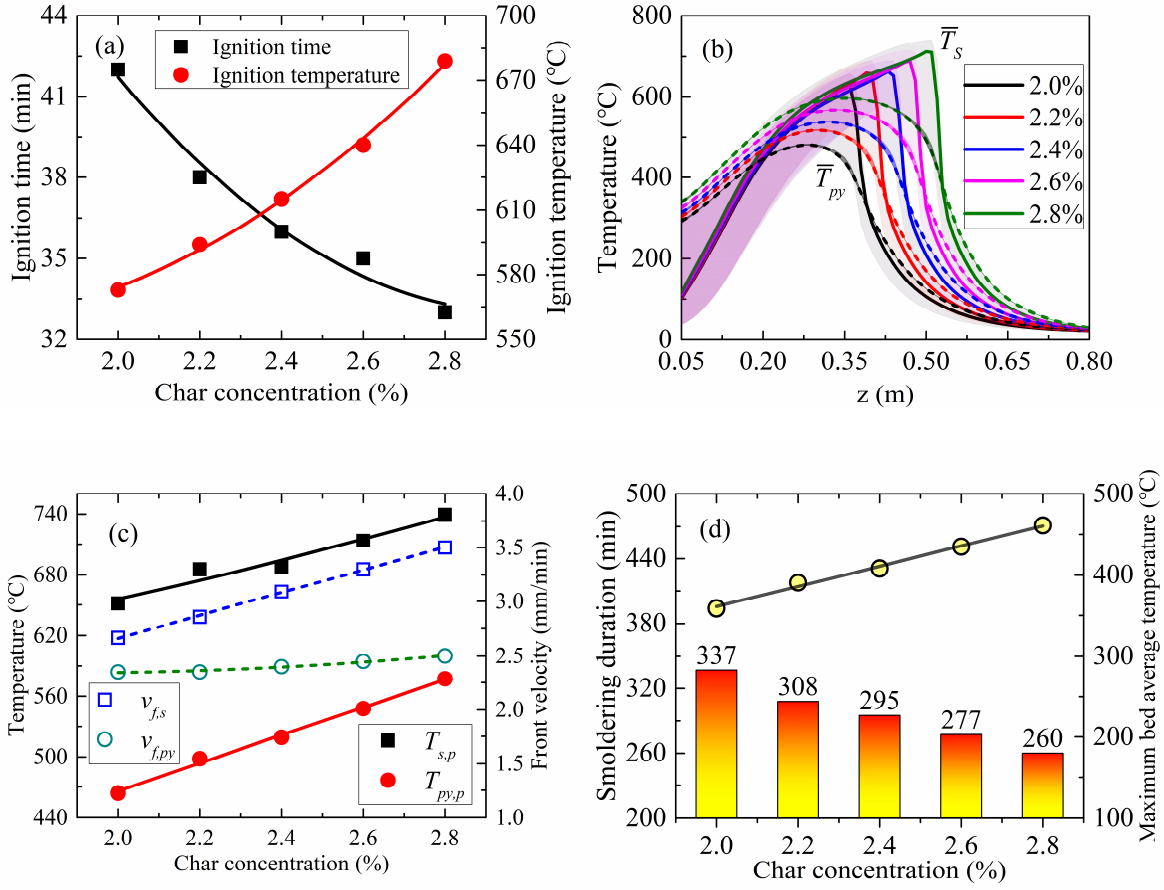

Fig. 5. Effect of char concentration on (a) ignition time and temperature, (b) longitudinal radial-mean T_s (solid line) and radial-mean T_{py} (dashed line) profiles at t=10800s, (c) average $T_{s,p}$ and $T_{py,p}$, and (d) smoldering duration and maximum pyrolysis bed average temperature.

3.4.Effect of air inlet velocity

Fig. 6 depicts the effect of air inlet velocity on the temperature distribution at ignition time. It can be concluded that there is no significant difference in the ignition locations under the air inlet velocities of 0.03–0.05m/s, all at z=0.030–0.035m. However, the ignition locations are

z=0.044m and z=0.161m under 0.06m/s and 0.07m/s, respectively. Higher air inlet velocities cause the solid to be excessively cooled by the convective heat transfer. Excessive convective cooling compels the maximum temperature at the inlet to decrease from 908°C to 842°C at the ignition time. The char at the lower region of the ignition point has not been completely reacted under 0.06m/s and 0.07m/s (Fig. A.4). An unburnt char region could be observed along the outer wall of the smoldering chamber under 0.05–0.07m/s due to the boundary heat loss and the excessive convective cooling (Fig. A.5) [37].

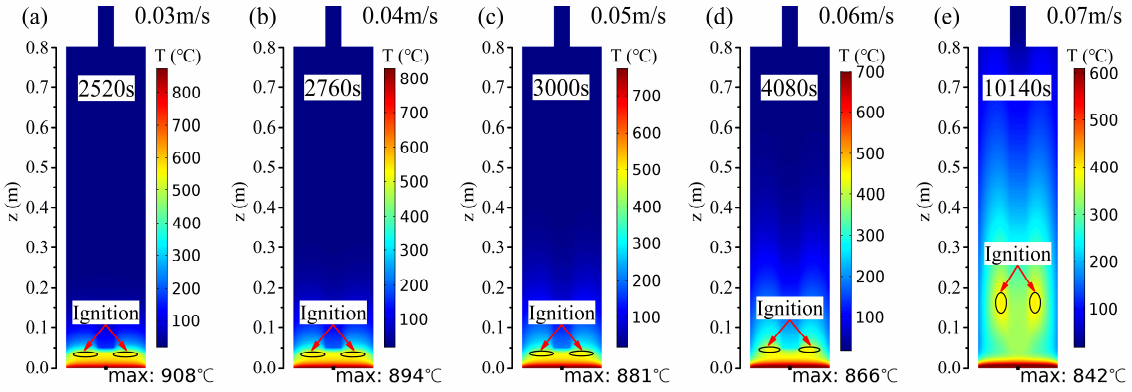

Fig. 6. Temperature distributions at ignition time under different air inlet velocities: (a) 0.03m/s; (b) 0.04m/s; (c) 0.05m/s; (d) 0.06m/s; (e) 0.07m/s.

Fig. 7a shows that increasing the air inlet velocity prolongs the ignition time from 42min to 169min and decreases the ignition temperature from 573°C to 399°C. The gas carries more energy out of the smoldering chamber at higher air inlet velocities, resulting in more external energy input, i.e., longer ignitor heating time for the ignition [12]. Fig. 7b demonstrates that the radial-mean peak T_S and T_{py} first increase (in the range of 0.03–0.04m/s) and then decrease (in the range of 0.05–0.07m/s) at t=10800s with the increasing air inlet velocity. It is noteworthy

255 that the peak T_S increases from 660°C at 0.03m/s to 673°C at 0.07m/s when the smoldering
256 propagates steadily (Fig. A.6), which is attributed to the increased local oxidation rate [38-39].
257 On the other hand, higher air inlet velocities result in less energy remaining in the solid before
258 smoldering propagates steadily due to the excessive convective cooling, leading to a decrease
259 in T_S at t=10800s (Fig. 7b).

260 Fig. 7c demonstrates that increasing the air inlet velocity decreases the average peak T_S by
261 140°C (651–512°C) and T_{py} by 31°C (464–433°C). Higher air inlet velocity can improve the
262 char oxidation rate due to the more oxygen supplied per unit time in the smoldering chamber
263 [12]. Accordingly, the consumed oxygen concentration decreases from 4.4% to 3.7% as the air
264 inlet velocity increases in the studied range (Fig. A.7). The local energy out rate is raised at
265 higher air inlet velocities, further increasing the front velocities of $v_{f,s}$ and $v_{f,py}$. Although the
266 smoldering front velocity $v_{f,s}$ has been increased, the higher air inlet velocity also causes the
267 ignition time to prolong, so the smoldering duration first decreases from 337min at 0.03m/s to
268 279min at 0.05m/s and then increases to 308min at 0.07m/s (Fig. 7d). The complex interaction
269 between the excessive convective cooling and the increased local oxidation rate causes the
270 smoldering bed average temperature to decrease from 336°C at 0.03m/s to 300°C at 0.06m/s
271 and then increase to 340°C at 0.07m/s (Fig. A.8). Accordingly, the pyrolysis bed average
272 temperature first reduces from 358°C to 326°C and then enhances to 363°C when the air inlet
273 velocity increases in the studied range (Fig. 7d). Altogether, it can be concluded that 0.04m/s is
274 the ideal air inlet velocity in the scenarios studied.

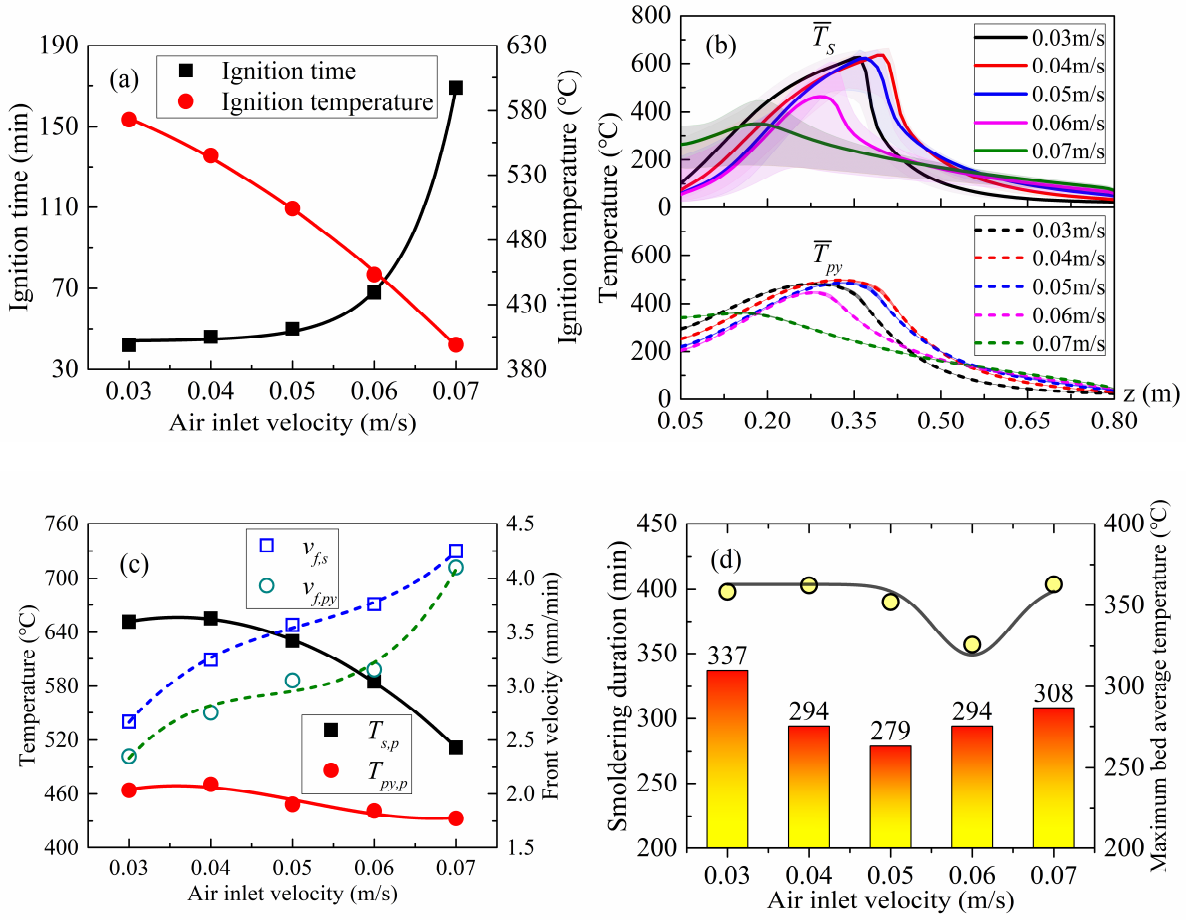

Fig. 7. Effect of air inlet velocity on (a) ignition time and temperature, (b) longitudinal radial-mean T_s (solid line) and radial-mean T_{py} (dashed line) profiles at t=10800s, (c) average $T_{s,p}$ and $T_{py,p}$, and (d) smoldering duration and maximum pyrolysis bed average temperature.

3.5.Effect of oxygen concentration

Fig. 8a reveals that increasing the oxygen concentration can shorten the ignition time by 18min (56–38min) and decrease the ignition temperature by 22°C (589–567°C). It should be noted that the oxygen is in excess in all the scenarios studied (Fig. A.9). The consumed oxygen increases from 3.3% to 5.0% with the increased oxygen concentration, attributed to higher char oxidation rates. Higher oxygen concentrations enhance the char oxidation rate and local energy

generation rate, thereby reducing the external energy input, i.e., shortening the time to ignite [40]. Lower ignition temperatures indicate that smoldering is more likely to occur at higher oxygen concentrations [41-42]. Moreover, there is no significant difference in the ignition locations at different oxygen concentrations, all at z=0.03–0.04m.

Fig. 8b shows that the radial-mean peak T_S and T_{py} have negligible sensitivities to the oxygen concentration, which agree with the findings in [12]. However, higher oxygen concentrations can push the temperature front forward, thus resulting in higher front velocities of $v_{f,s}$ and $v_{f,py}$ due to the increased local energy out rate (Fig. 8c) [22,38,43]. The increased local energy out rate also reduces the local heat accumulation stored in the sand. On the other hand, the thickness of the smoldering front decreases when the oxygen concentration increases in the studied range (Fig. A.10), leading to a slight decrease in the peak temperature (Fig. A.11) [12], further lowering the average peak T_S and T_{py} (Fig. 8c). Nonetheless, higher oxygen concentrations increase the smoldering bed average temperature (Fig. A.12), thus improving the pyrolysis bed average temperature from 346°C to 366°C and shortening the smoldering duration from 404min to 301min (Fig. 8d).

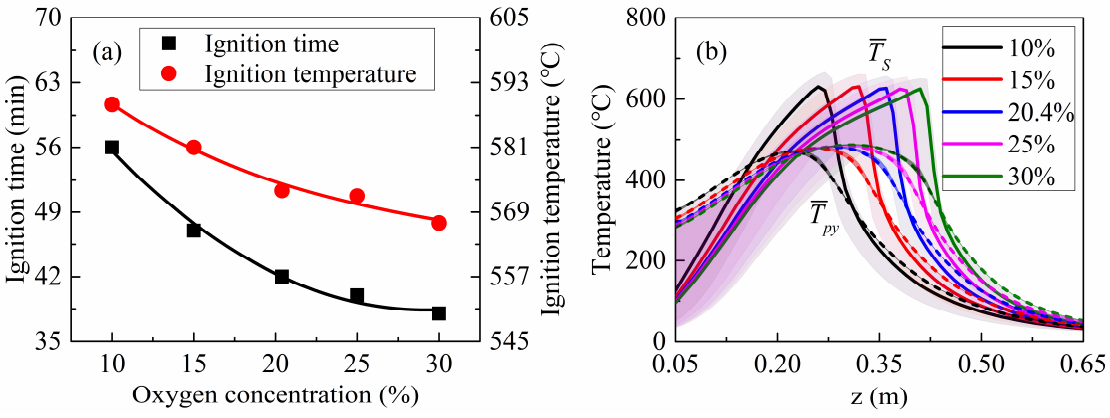

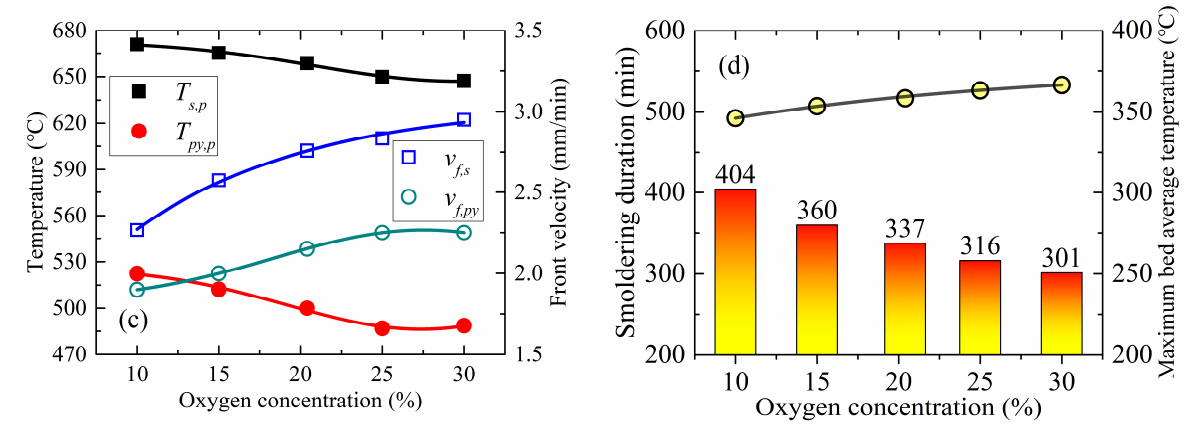

Fig. 8. Effect of oxygen concentration on (a) ignition time and temperature, (b) longitudinal radial-mean T_s (solid line) and radial-mean T_{py} (dashed line) profiles at t=10800s, (c) average $T_{s,p}$ and $T_{py,p}$, and (d) smoldering duration and maximum pyrolysis bed average temperature.

4. Conclusions

This study developed a numerical model for the smoldering-driven pyrolysis reactor. The reactor consists of a smoldering chamber for contaminated sand remediation and a pyrolysis chamber for waste valorization. The primary objective of this study is to verify the feasibility of this reactor and evaluate its thermal performance. It should be noted that no reactants (wastes) were added to the pyrolysis chamber. The reactor's thermal performance was evaluated through four aspects: (i) the ignition time indicating the amount of external energy that needs to be input, (ii) the average peak temperature indicating the temperature required for the pyrolysis of different wastes, (iii) the smoldering duration indicating the time it takes for the pyrolysis of wastes, and (iv) the maximum pyrolysis bed average temperature indicating the amount of energy received by the pyrolysis bed. This study's main findings and conclusions can be outlined as described below.

The contaminant (char) in the sand could be eliminated via smoldering, which was a self-sustaining process after ignition. The heatwave generated in the smoldering chamber could heat the pyrolysis chamber through the boundary heat flux.

Higher char concentrations decreased the ignition time, increased the average peak temperature, shortened the smoldering duration, and enhanced the maximum pyrolysis bed average temperature, which were all beneficial to the improvement of the thermal performance of the reactor.

The increment in air inlet velocity led to a significant increase in ignition time and a decrease in average peak temperature. The complex interaction between the excessive convective cooling and the increased local oxidation rate caused the smoldering duration and pyrolysis bed average temperature to first reduce and then enhance when the air inlet velocity increased in the studied range. Considering all the above effects, 0.04m/s was the ideal air inlet velocity in the scenarios studied.

Increased oxygen concentration shortened the ignition time and smoldering duration and increased the maximum pyrolysis bed average temperature. At the same time, the average peak temperature decreased when the oxygen concentration increased in the studied range, indicating that higher oxygen concentrations are not suitable for wastes that require higher temperatures to pyrolyze.

Acknowledgements

This work was supported by the China Scholarship Council (CSC) program (No.

201906120036). The authors appreciate Dr. M.A.B. Zanoni for providing experimental data and valuable discussion. The authors greatly acknowledge the anonymous reviewers' kind and helpful suggestions.

Conflict of interest

The authors declare no competing financial interest.

References

[1] Torero, J.L., Gerhard, J.I., Martins, M.F., Zanoni, M.A., Rashwan, T.L. and Brown, J.K., 2020. Processes defining smouldering combustion: Integrated review and synthesis. Progress in Energy and Combustion Science, 81, p.100869. https://doi.org/10.1016/j.pecs.2020.100869

[2] Gianfelice, G. and Canu, P., 2021. On the mechanism of single pellet smouldering combustion. Fuel, 301, p.121044. https://doi.org/10.1016/j.fuel.2021.121044

[3] Wang, Z., Liu, N., Yuan, H., Chen, H., Xie, X., Zhang, L. and Rein, G., 2022. Smouldering and its transition to flaming combustion of polyurethane foam: An experimental study. Fuel, 309, p.122249. https://doi.org/10.1016/j.fuel.2021.122249

[4] Duchesne, A.L., Brown, J.K., Patch, D.J., Major, D., Weber, K.P. and Gerhard, J.I., 2020. Remediation of PFAS-contaminated soil and granular activated carbon by smoldering combustion. Environmental Science & Technology, 54(19), pp.12631-12640. https://doi.org/10.1021/acs.est.0c03058

[5] Bittencourt, F.L.F., Martins, M.F., Orlando, M.T.D. and Galvão, E.S., 2022. The proof-of-concept of a novel feces destroyer latrine. Journal of Environmental Chemical Engineering, 10(1), p.106827. https://doi.org/10.1016/j.jece.2021.106827

[6] Yermán, L., Wall, H. and Torero, J.L., 2017. Experimental investigation on the destruction rates of organic waste with high moisture content by means of self-sustained smoldering combustion. Proceedings of the Combustion Institute, 36(3), pp.4419-4426. https://doi.org/10.1016/j.proci.2016.07.052

[7] Sun, Y., Bai, F., Liu, B., Liu, Y., Guo, M., Guo, W., Wang, Q., Lü, X., Yang, F. and Yang, Y., 2014. Characterization of the oil shale products derived via topochemical reaction method. Fuel, 115, pp.338-346. https://doi.org/10.1016/j.fuel.2013.07.029

[8] Yermán, L., Cormier, D., Fabris, I., Carrascal, J., Torero, J.L., Gerhard, J.I. and Cheng, Y.L., 2017. Potential bio-oil production from smouldering combustion of faeces. Waste and biomass valorization, 8(2), pp.329-338. https://doi.org/10.1007/s12649-016-9586-1

[9] Zhao, C., Li, Y., Gan, Z. and Nie, M., 2021. Method of smoldering combustion for refinery oil sludge treatment. Journal of Hazardous Materials, 409, p.124995. https://doi.org/10.1016/j.jhazmat.2020.124995

[10] Li, X., Kær, S.K., Condra, T. and Yin, C., 2021. A detailed computational fluid dynamics model on biomass pellet smoldering combustion and its parametric study. Chemical Engineering Science, 231, p.116247. https://doi.org/10.1016/j.ces.2020.116247

[11] Zanoni, M.A., Wang, J. and Gerhard, J.I., 2021. Understanding pressure changes in smouldering thermal porous media reactors. Chemical Engineering Journal, 412, p.128642. https://doi.org/10.1016/j.cej.2021.128642

[12] Zanoni, M.A., Torero, J.L. and Gerhard, J.I., 2019. Delineating and explaining the limits of self-sustained smouldering combustion. Combustion and Flame, 201, pp.78-92. https://doi.org/10.1016/j.combustflame.2018.12.004

[13] Chen, H., Rein, G. and Liu, N., 2015. Numerical investigation of downward smoldering combustion in an organic soil column. International Journal of Heat and Mass Transfer, 84, pp.253-261. https://doi.org/10.1016/j.ijheatmasstransfer.2015.01.016

391 [14] Kinsman, L., Torero, J.L. and Gerhard, J.I., 2017. Organic liquid mobility induced by
392 smoldering remediation. Journal of Hazardous materials, 325, pp.101-112.
393 https://doi.org/10.1016/j.jhazmat.2016.11.049
394 [15] Duque, J.V.F., Martins, M.F., Bittencourt, F.L. and Debenest, G., 2021. Relevant aspects of
395 propagating a combustion front in an annular reactor for out-of-bed heat recovery.
396 Experimental Thermal and Fluid Science, p.110575.
397 https://doi.org/10.1016/j.expthermflusci.2021.110575
398 [16] Ronda, A., Della Zassa, M., Gianfelice, G., Iáñez-Rodríguez, I. and Canu, P., 2019.
399 Smouldering of different dry sewage sludges and residual reactivity of their intermediates.
400 Fuel, 247, pp.148-159. https://doi.org/10.1016/j.fuel.2019.03.026
401 [17] Della Zassa, M., Ronda, A., Gianfelice, G., Zerlottin, M. and Canu, P., 2019. Scale effects
402 and mechanisms ruling the onset of wastewater sludges self-heating. Fuel, 256, p.115876.
403 https://doi.org/10.1016/j.fuel.2019.115876
404 [18] Da Lio, L., Castello, P., Gianfelice, G., Cavalli, R. and Canu, P., 2021. Effective energy
405 exploitation from horse manure combustion. Waste Management, 128, pp.243-250.
406 https://doi.org/10.1016/j.wasman.2021.04.035
407 [19] Feng, C., Cheng, M., Gao, X., Qiao, Y. and Xu, M., 2021. Occurrence forms and
408 leachability of inorganic species in ash residues from self-sustaining smouldering
409 combustion of sewage sludge. Proceedings of the Combustion Institute, 38(3), pp.4327-
410 4334. https://doi.org/10.1016/j.proci.2020.06.008
411 [20] Song, Z., He, T., Li, M., Wu, D. and You, F., 2022. Self-sustaining smoldering as a novel

disposal approach for food waste with high moisture content. Fuel Processing Technology, 228, p.107144. https://doi.org/10.1016/j.fuproc.2021.107144

[21] Fabris, I., Cormier, D., Gerhard, J.I., Bartczak, T., Kortschot, M., Torero, J.L. and Cheng, Y.L., 2017. Continuous, self-sustaining smouldering destruction of simulated faeces. Fuel, 190, pp.58-66. https://doi.org/10.1016/j.fuel.2016.11.014

[22] Lin, S., Yuan, H. and Huang, X., 2022. A computational study on the quenching and near-limit propagation of smoldering combustion. Combustion and Flame, 238, p.111937. https://doi.org/10.1016/j.combustflame.2021.111937

[23] Li, X., Yin, C., Kær, S.K. and Condra, T., 2020. A detailed pyrolysis model for a thermally large biomass particle. Fuel, 278, p.118397. https://doi.org/10.1016/j.fuel.2020.118397

[24] Pan, R., Martins, M.F. and Debenest, G., 2021. Pyrolysis of waste polyethylene in a semi-batch reactor to produce liquid fuel: Optimization of operating conditions. Energy Conversion and Management, 237, p.114114. https://doi.org/10.1016/j.enconman.2021.114114

[25] Pan, R., Martins, M.F. and Debenest, G., 2022. Optimization of oil production through ex-situ catalytic pyrolysis of waste polyethylene with activated carbon. Energy, p.123514. https://doi.org/10.1016/j.energy.2022.123514

[26] Pan, R., Zan, Y. and Debenest, G., 2022. Oil production from waste polyethylene and polystyrene co-pyrolysis: Interactions of temperature and carrier gas flow rate. Journal of Environmental Chemical Engineering, p.107555. https://doi.org/10.1016/j.jece.2022.107555

[27] Duque, J.V.F., Bittencourt, F.L., Martins, M.F. and Debenest, G., 2021. Developing a combustion-driven reactor for waste conversion. Energy, 237, p.121489. https://doi.org/10.1016/j.energy.2021.121489

[28] Mazloum, S., Awad, S., Allam, N., Aboumsallem, Y., Loubar, K. and Tazerout, M., 2021. Modelling plastic heating and melting in a semi-batch pyrolysis reactor. Applied Energy, 283, p.116375. https://doi.org/10.1016/j.apenergy.2020.116375

[29] Lougou, B.G., Shuai, Y., Pan, R., Chaffa, G. and Tan, H., 2018. Heat transfer and fluid flow analysis of porous medium solar thermochemical reactor with quartz glass cover. International Journal of Heat and Mass Transfer, 127, pp.61-74. https://doi.org/10.1016/j.ijheatmasstransfer.2018.06.153

[30] Pan, R., Lougou, B.G., Shuai, Y., Zhang, G. and Zhang, H., 2019. Heat transfer modeling of a high-temperature porous-medium filled solar thermochemical reactor for hydrogen and synthesis gas production. Journal of Heat Transfer, 141(2). https://doi.org/10.1115/1.4041707

[31] Shi, X., Chen, X., Zhang, Y., Zhang, Y., Shi, Z., Che, B. and Xia, S., 2021. Characteristics of self–ignition and smoldering of coal dust layer under inclination conditions. Process Safety and Environmental Protection, 156, pp.1-16. https://doi.org/10.1016/j.psep.2021.09.048

[32] Pozzobon, V., Baud, G., Salvador, S. and Debenest, G., 2017. Darcy scale modeling of smoldering: impact of heat loss. Combustion Science and Technology, 189(2), pp.340-365. https://doi.org/10.1080/00102202.2016.1214585

[33] Zanoni, M.A., Torero, J.L. and Gerhard, J.I., 2017. Determination of the interfacial heat transfer coefficient between forced air and sand at Reynold's numbers relevant to smouldering combustion. International Journal of Heat and Mass Transfer, 114, pp.90-104. https://doi.org/10.1016/j.ijheatmasstransfer.2017.06.020

[34] Ding, K., Xiong, Q., Zhong, Z., Zhong, D. and Zhang, Y., 2020. CFD simulation of combustible solid waste pyrolysis in a fluidized bed reactor. Powder Technology, 362, pp.177-187. https://doi.org/10.1016/j.powtec.2019.12.011

[35] Wang, J., Xing, W., Huang, X., Jin, X., Yu, H., Wang, J., Song, L., Zeng, W. and Hu, Y., 2020. Smoldering of storage rice: Effect of moldy degree and moisture content. Combustion Science and Technology, pp.1-13. https://doi.org/10.1080/00102202.2020.1813120

[36] Wu, D., Song, Z., Schmidt, M., Zhang, Q. and Qian, X., 2019. Theoretical and numerical study on ignition behaviour of coal dust layers on a hot surface with corrected kinetic parameters. Journal of hazardous materials, 368, pp.156-162. https://doi.org/10.1016/j.jhazmat.2019.01.032

[37] Baud, G., Salvador, S., Debenest, G. and Thovert, J.F., 2015. New Granular Model Medium To Investigate Smoldering Fronts Propagation—Experiments. Energy & Fuels, 29(10), pp.6780-6792. https://doi.org/10.1021/acs.energyfuels.5b01325

[38] Hadden, R.M., Rein, G. and Belcher, C.M., 2013. Study of the competing chemical reactions in the initiation and spread of smouldering combustion in peat. Proceedings of the Combustion Institute, 34(2), pp.2547-2553.

https://doi.org/10.1016/j.proci.2012.05.060

[39] Pan, R. and Debenest, G., 2022. Numerical investigation of a novel smoldering-driven reactor for plastic waste pyrolysis. Energy Conversion and Management, 257, p.115439. https://doi.org/10.1016/j.enconman.2022.115439

[40] Leach, S.V., Rein, G., Ellzey, J.L., Ezekoye, O.A. and Torero, J.L., 2000. Kinetic and fuel property effects on forward smoldering combustion. Combustion and flame, 120(3), pp.346-358. https://doi.org/10.1016/S0010-2180(99)00089-9

[41] Belcher, C.M. and McElwain, J.C., 2008. Limits for combustion in low O2 redefine paleoatmospheric predictions for the Mesozoic. Science, 321(5893), pp.1197-1200. https://doi.org/10.1126/science.1160978

[42] Belcher, C.M., Mander, L., Rein, G., Jervis, F.X., Haworth, M., Hesselbo, S.P., Glasspool, I.J. and McElwain, J.C., 2010. Increased fire activity at the Triassic/Jurassic boundary in Greenland due to climate-driven floral change. Nature Geoscience, 3(6), pp.426-429. https://doi.org/10.1038/ngeo871

[43] Belcher, C.M., Yearsley, J.M., Hadden, R.M., McElwain, J.C. and Rein, G., 2010. Baseline intrinsic flammability of Earth's ecosystems estimated from paleoatmospheric oxygen over the past 350 million years. Proceedings of the National Academy of Sciences, 107(52), pp.22448-22453. https://doi.org/10.1073/pnas.1011974107